Physics of Electrostatic Projection Revealed by High-Speed Video Imaging

Arash Sayyah,[1] Mohammad Mirzadeh,[1] Yi Jiang,[2] Warren V. Gleason,[2] William C. Rice,[2] and Martin Z. Bazant[1,3,*]

[1] *Department of Chemical Engineering, Massachusetts Institute of Technology, Cambridge, Massachusetts 02139, USA*

[2] *Saint-Gobain Research North America, Northborough, Massachusetts 01532, USA*

[3] *Department of Mathematics, Massachusetts Institute of Technology, Cambridge, Massachusetts 02139, USA*

(Received 20 November 2019; revised manuscript received 8 March 2020; accepted 10 March 2020; published 30 March 2020)

Processes based on electrostatic projection are used extensively in industry, e.g., for mineral separations, electrophotography, or manufacturing of coated abrasives, such as sandpaper. Despite decades of engineering practice, there are still unanswered questions. In this paper, we present a comprehensive experimental study of the projection process of more than 1500 individual spherical alumina particles with a nominal size of 500 μm, captured by high-speed video imaging and digital image analysis. Based on flight trajectories of approximately 1100 projected particles, we determine the acquired charge and dynamics as a function of the relative humidity (RH) and the electric field intensity and compare the results with classical theories. For RH levels of 50% and above, more than 85% of distributed particles are projected, even when the electric field intensity is at its minimum level. This suggests that, beyond a critical value of the electric field intensity, the RH plays a more critical role in the projection process. We also observe that the charging time is reduced dramatically for RH levels of 50% and above, possibly due to the buildup of thin water films around the distributed particles, which can facilitate charge transfer. In contrast, projected particles at the 30% RH level exhibit excessive amounts of electric charge, between 2 and 4 times than that of the saturation value, which might be attributed to triboelectric charging effects. Finally, the physics of electrostatic projection is compared and contrasted with those of induced-charge electrokinetic phenomena, which share similar field-square scaling, as the applied electric field acts on its own induced charge to cause particle motion.

DOI: 10.1103/PhysRevApplied.13.034071

I. INTRODUCTION

Electric-field-driven motion of particles is ubiquitous in many physical, chemical, and biological systems. Electrophoresis of suspended charged colloids in a uniform electric field is a familiar example [1], which has diverse applications ranging from DNA separation [2,3] to material processing via electrophoretic deposition [4,5]. Electrophoresis of charged droplets is similarly relevant to mass spectrometry via electrospray ionization [6], high-precision inkjet printing [7], electrostatic phase separation [8], deemulsification and dehydration in petroleum engineering [9], and droplet manipulation in microfluidic devices [10,11].

Electrostatic interactions could also occur with uncharged but polarizable particles. In particular, induced-charge electro-osmosis (ICEO) is a general nonlinear phenomenon whereby an electric field induces an ionic charge cloud around polarizable surfaces and subsequently acts upon it, which results in fluid flow and a particle velocity that scales quadratically with the electric field [12–17]. A unique feature of ICEO is that, due quadratic scaling, the fluid velocity is unaffected by the polarity of the applied electric field. However, a net fluid pumping or particle motion generally requires a broken symmetry [18], e.g., in the particle shape, the surface properties, and/or the proximity to a wall [19], as in induced-charge electrophoresis (ICEP) of metallodielectric Janus particles [20,21]. Particle motion is also possible in nonuniform electric fields via dielectrophoresis (DEP), which scales with the gradient of the square of the electric field strength due to interaction between the electric field gradient and the induced dipole moment [22]. These nonlinear interactions often lead to fascinating collective behavior in colloidal suspensions. For instance, electric fields tend to direct self-assembly of particles near electrodes to form colloidal crystals [23–30]. These structures form in response to ICEO flows that entrap nearby particles despite repulsive dipolar interactions [31–33]. Similarly, large electric fields can trigger dipole-dipole attraction between suspending particles, leading to the formation of long chains along the

*bazant@mit.edu

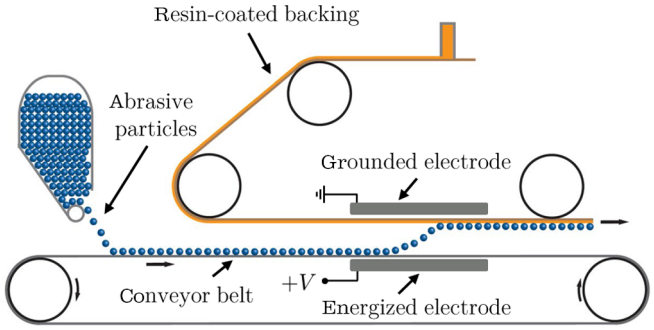

FIG. 1. A schematic of an industrial process relying on electrostatic projection for manufacturing coated abrasives. A conveyor belt transports abrasive particles from a particle feeder over an electrode, where a large electric field is applied. The particles acquire electric charge through an induction mechanism and feel an upward Coulomb force. Because the induced charge is proportional to the electric field [see Eq. (1)], the Coulomb force is always repulsive, independent of the electric field direction.

electric field that impede fluid motion. This is the main idea behind electrorheological (ER) fluids, where electric fields are used to tune bulk viscosity [34–37].

In both ICEP and DEP particle motion, net charge plays a secondary role, and the nonlinear electrokinetic phenomena originate from an induced dipole on the particle. However, charge transfer is possible if polarized particles are brought into direct contact with each other, a wall, or an electrode—the case of interest here. This inductive charging mechanism, analogous to the charging of a two-plate capacitor, proceeds until either both surfaces reach the same electric potential or contact is terminated. When the particle is sufficiently charged, a Coulomb force pushes the surfaces apart and the electric field drives an electrophoretic motion toward the opposite electrode. Both the particle charge and the direction of electrophoretic motion reverse upon contact with the opposite electrode and an oscillatory motion ensues. Such a phenomenon has been utilized in manipulating particles and in droplet motion in microfluidic devices using a dc electric field [38–42]. However, when the suspending medium has a sufficiently low viscosity, the Coulomb force can easily overcome the drag force or a particle's weight and results in electrostatic projection (see Fig. 1). Here, similar to ICEP, the electric field both induces a net charge on the particle and subsequently acts upon it, leading to a repulsive Coulomb force that scales quadratically with the electric field. In this sense, it could be argued that electrostatic projection can be thought of as an extreme case of induced-charge electrokinetic phenomena.

Electrophotography [43,44] and mineral separation and processing [45] are two examples that routinely rely on electrostatic projection. Another widely used and yet obscure application of this technique is in manufacturing of coated abrasives [46–49]. In this industrial process, an excessive number of particles (abrasive grains) are fed onto a conveyor belt that goes through a narrow air gap below a moving adhesive web, where a high-intensity magnetic or electrostatic field is applied. Particles acquire electric charge, traverse the narrow air gap, and lodge in the adhesive web. Despite the extensive use of this technique, a more comprehensive understanding of this process can be helpful in optimizing the process and creating a final product with the desired features. It is important to know, for instance, how the shape, size, density, and material properties of particles contribute in the projection process or how particles behave when they are exposed in different relative humidity (RH) conditions and electric field intensities.

Wu *et al.* [50] ran electrostatic-particle-projection experiments with particles with identical composition but having three different sizes, distributed on a belt. The motion of the particles was recorded using a high-speed digital-imaging system. A key question answered in this study was the physical origin of the charge acquired by the particles. Although particles always have a preexisting surface charge, influenced by tribological and electrostatic conditions prior to entering the projection zone, it was shown in this case that induced charge transferred from the belt to particles is primarily responsible for electrostatic projection. In this mechanism, each particle and the belt effectively behave as two plates of a capacitor, which become separated under the right conditions (to be elaborated further below). Their experimental results were in good agreement with a simple model, which assumes that induced charge is distributed on the entire surface of each particle. In addition, they found that the charging time and charge on a freely levitating particle mainly depend on the electric field strength, particle size, and resistivity. They also observed that projection of conducting aluminum particles was independent of the RH.

In a later study, Wu *et al.* [51] examined the impact of the electric field intensity on the induction charge of semiconducting particles. They conducted their projection experiments under four electric field intensities on particles with a 156-μm mass mean diameter. They concluded that the acquired electric charge of particles is a function of both the electric field intensity and the charging time. Furthermore, they found that increasing the electric field intensity does not necessarily contribute to a higher number of projected particles. Based on these findings, they continued their study in Ref. [52], where the projection of irregular-shaped alumina particles and spherical glass beads with a size range of $42 - 390$ μm were examined at different electric field intensities. By performing charge-to-mass ratio measurements, they found that the mean size of the projected particles increased with the electric field intensity and that particles with a larger surface area acquired more electric charge. To more accurately calculate the average charge per particle

based on the charge-to-mass measurements, Wu *et al.* [53] studied the shape and size of irregular-shaped particles through surface-mean-diameter and volume-mean-diameter parameters. When they applied their new method to a study of the induction charging of irregular-shaped and spherical particles, the results of the new method were in good agreement with the theoretical predictions.

Sow *et al.* [54] conducted a series of experiments on electrostatic projection of four types of spherical particles—aluminum, polytetrafluoroethylene (PTFE), nylon, and soda-lime glass—at low and high RH levels. Unlike the behavior of the aluminum and PTFE particles, which were consistent with the conducting- and insulating-particle models, respectively, they surprisingly observed that nylon and soda-lime glass were projected according to the conducting-particle model at low RH levels and the insulating-particle model at high RH levels. They concluded that at high RH levels, due to the hydrophilic nature of nylon and soda-lime glass, a conducting layer of water formed on their surfaces that facilitated charge transfer and, accordingly, they resembled the conducting-particle model.

In this paper, we examine the projection process of more than 1500 alumina particles under different operational conditions using a high-speed video imaging setup. This is a comprehensive experimental study of electrostatic projection of abrasive particles. We find that the projection performance greatly depends on the RH, with more than 85% of particles being projected at 50% or higher RH levels. By analyzing high-speed video footage, we are able to estimate the acquired charge of individual particles and the amount of time required for the charge transfer to occur. At 40% and higher RH, the total charge accumulated on each projected particle does not seem to vary with the RH value, but the charging time is dramatically reduced at higher RH values. We hypothesize this could be due to the formation of thin water films around particles, which facilitate charge transfer and lower the contact resistance. Conversely, the electric field intensity does not seem to considerably affect the charging time and primarily only affects the overall particle charge.

II. THEORETICAL BACKGROUND

When a particle is placed in an external electric field, it can be polarized. If the particle is brought into contact with a conductive surface (e.g., an electrode), free charges can transfer between the particle and the surface and the particle can acquire a net charge. The sign of the net charge depends on the potential difference between the particle and the surface. This is illustrated schematically in Fig. 3, where several alumina particles acquire an electric charge when the lower electrode is biased with a voltage. Here, we focus on a positive bias voltage to remain consistent with the experiments but similar mechanisms hold for a negative bias voltage. The charging process proceeds until either the particle levitates and is projected off the lower electrode's surface due to a strong Coulomb force or the particle reaches the same potential with the electrode and no more charge can be transferred. In the latter case, the so-called "saturation" or "Maxwell" charge is reached, which for a spherical particle of radius R in an electric field $E = V/H$ is given by [22,55–57]

$$Q_s = \frac{2\pi^3}{3}\varepsilon_m R^2 E. \tag{1}$$

Here, ε_m denotes the permittivity of the surrounding medium, which in our experiments is that of air, i.e., $\varepsilon_m \approx 8.85 \times 10^{-12}$ F/m, V is the applied voltage, and H is the length of the air gap. The saturation charge is calculated by assuming that the spherical particle is a perfect conductor sitting on an ideal flat electrode that is applying a uniform electric field in the half space, which is equivalent to the (equal and opposite) "capacitor" charge on a pair of touching conducting spheres in a uniform background field everywhere, by the method of images.

Equation (1) gives the maximum transferable charge by induction. The actual charge of a particle may, however, be different for several reasons. Undercharging is possible if the rate of charge transfer is relatively slow, so that the particle may lift off before charging is complete. Indeed, we observe undercharging during the majority of our experiments, especially at high electric field intensities. Similar undercharging events involving metallic particles and water droplets have recently been attributed to localized melting of the electrode surface at high current density and electrohydrodynamic instabilities that impede charge transfer [58,59]. Other effects such as nonuniform charge accumulation might also affect the particle charge and the electrostatic force between the particle and the electrode [22].

The electrostatic force acting on a charged particle near a conductive surface may be written as [22]

$$F_e = -\alpha\left(\frac{Q^2}{4\pi\varepsilon_m R^2}\right) + \beta QE - 4\gamma\pi\varepsilon_m R^2 E^2, \tag{2}$$

where the first and last terms represent the attractive image and dipole forces, respectively, and the second term is the familiar Coulomb repulsion. The coefficients α, β, and γ generally depend on the relative polarizability of the particle and the suspending medium as well as the particle distance to the electrode's surface. Simple expressions are available for weakly polarizable particles ($\varepsilon_p/\varepsilon_m < 4$) [22]. However these expressions are not accurate for the particles in our experiments due to the relatively large dielectric coefficient ($\varepsilon_p/\varepsilon_m \approx 10$). Instead, we use the method of multipolar expansion [60] to compute the coefficients in Eq. (2). This is achieved by first computing the

electrostatic force for a range of particle charges and then fitting Eq. (2) to obtain the unknown coefficients. For the particles in our study, these coefficients are found to be

$$\alpha \approx 0.20, \quad \beta \approx 1.91, \quad \gamma \approx 0.85. \tag{3}$$

Equation (2) suggests that electrostatic projection is only possible for a range of particle charges, i.e., $Q_{\min} < Q < Q_{\max}$. This is also evident from Fig. 2, which illustrates the electrostatic force on the particle as a function of its charge. When the particle is not sufficiently charged ($Q < Q_{\min}$), dipole attraction dominates Coulomb repulsion. Similarly, for overly charged particles ($Q > Q_{\max}$), image attraction dominates Coulomb repulsion. In both cases, electrostatic forces are attractive ($F_e < 0$) and projection is not possible. For moderately charged particles, projection occurs for sufficiently large electric field intensities ($E > E_{\min}$), when the electrostatic force overcomes the weight of the particle:

$$F_e > W = \mathrm{mg}. \tag{4}$$

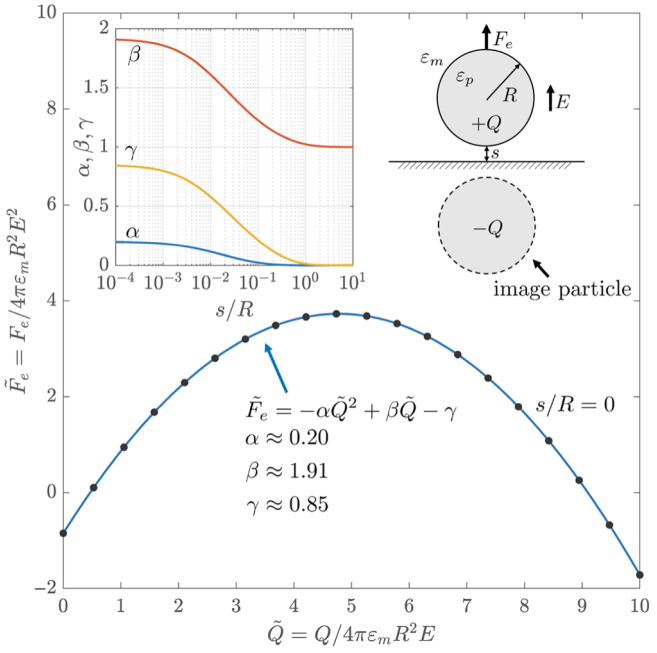

FIG. 2. The electrostatic force felt by a particle near a conductive surface is the sum of the image, Coulomb, and dipole contributions, resulting in the quadratic expression in Eq. (2). The electrostatic interaction is dominated by image forces for highly charged particles ($\tilde{Q} > \tilde{Q}_{\max}$) and dipole forces for very strong fields ($\tilde{Q} < \tilde{Q}_{\min}$), resulting in electrostatic adhesion ($\tilde{F}_e < 0$). Particle projection is possible ($\tilde{F}_e > 0$) for moderately charged particles, i.e., $\tilde{Q}_{\min} < \tilde{Q} < \tilde{Q}_{\max}$. The inset illustrates the variation of different contributions to the electrostatic force. The coefficients are found by fitting Eq. (2) (in nondimensional form) to numerical values computed using the method of multipolar expansion. As the particle levitates, the image and dipole forces quickly tend to zero and the electrostatic force is simply given by the Coulomb force, i.e., $F_e = QE$.

The minimum required electric field is computed from Eqs. (2) and (4):

$$\tilde{E}_{\min}(\tilde{Q}) = \frac{E_{\min}}{E_p} = \frac{1}{\sqrt{-\alpha\tilde{Q}^2 + \beta\tilde{Q} - \gamma}}, \tag{5}$$

where $\tilde{Q} = Q/4\pi\varepsilon_m R^2 E$ and $E_p = \sqrt{\rho_m g R/3\varepsilon_m}$ is a typical field strength needed for projection of a particle with density ρ_m. For the particles in our experiments, $E_p \approx 10\,\mathrm{kV/cm}$. In particular, electrostatic projection is not possible if $\tilde{E} < \tilde{E}_{\mathrm{cr}}$, where the critical field intensity, $\tilde{E}_{\mathrm{cr}}$, is given via

$$\tilde{E}_{\mathrm{cr}} = \frac{1}{\sqrt{\beta^2/4\alpha - \gamma}} \approx 0.52. \tag{6}$$

Alternatively, Eq. (5) may be expressed in terms of the minimum required charge ($\tilde{Q}_{\min}$) for projection to occur:

$$\tilde{Q}_{\min}(\tilde{E}) = \frac{\beta - \sqrt{\beta^2 - 4\alpha(\gamma + 1/\tilde{E}^2)}}{2\alpha}, \quad \tilde{E} \geq \tilde{E}_{\mathrm{cr}}. \tag{7}$$

Projection is not possible if $\tilde{Q} < \tilde{Q}_{\min}$. In our experiments, we estimate the charge acquired by a particle by analyzing the flight trajectory of the particle and compare the result with the minimum required charge from Eq. (7).

Once the particle is in flight, we only consider the Coulombic contribution to the electrostatic force. This is justified since the image and dipole forces quickly tend to zero when the particle distance from the electrode's surface is comparable with its size (see Fig. 2). Therefore, the particle trajectory satisfies

$$m\frac{d^2y}{dt^2} = QE - W - F_D, \tag{8}$$

where F_D is the drag force, which depends on the particle velocity. In our experiments, the average particle velocity may be estimated from the flight time (see Fig. 9) and is roughly $U_{\mathrm{avg}} \sim 0.5$ m/s, resulting in an average particle Reynolds number of $\mathrm{Re} \sim 20$. Therefore, the ratio of the drag force to the particle weight may be estimated as

$$\frac{F_D}{W} \sim \frac{\rho_{\mathrm{air}} U_{\mathrm{avg}}^2 R^2}{\rho_m R^3 g} \sim \frac{\rho_{\mathrm{air}}}{\rho_m}\frac{U_{\mathrm{avg}}^2}{Rg} \approx 0.03, \tag{9}$$

indicating that the drag force may safely be ignored in our analysis. Therefore, particles essentially follow a parabolic trajectory, i.e., $y(t) = (QE - \mathrm{mg})t^2/2m$. In our experiments, we estimate the electric charge (Q) for each particle by curve fitting its flight trajectory as recorded by a high-speed video camera (see Fig. 3). This value is then compared against the theoretical saturation charge Q_s given via Eq. (1) as well as the minimum projection charge $Q_{\min}$ given via Eq. (7).

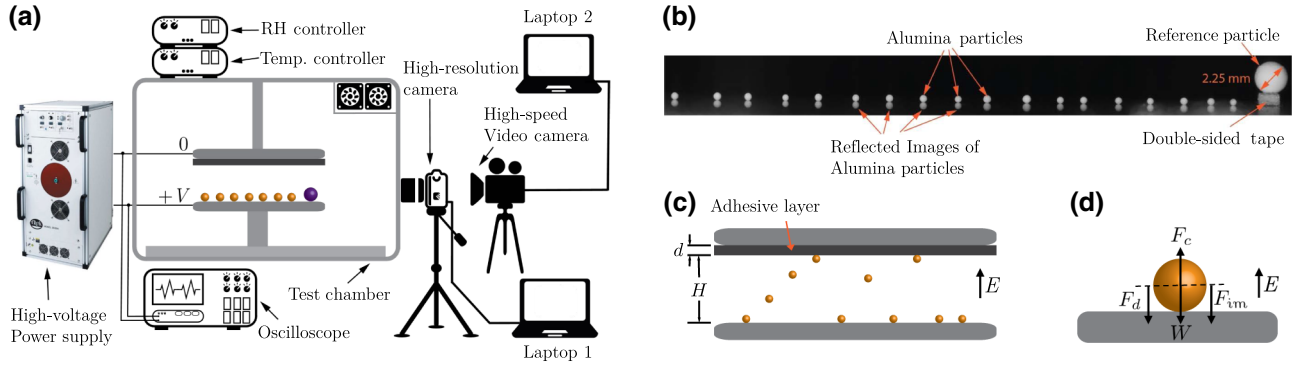

FIG. 3. (a) The experimental setup used in this study. After placement of spherical alumina particles in one straight line adjacent to the reference particle (depicted using a different color), the high-resolution camera takes a still image of the arrangement for further processing. Next, the high-voltage power supply is turned on and projection of particles is recorded using the high-speed video camera within a 5-s recording window. The RH controller and the temperature controller set the predetermined conditions for the environmentally controlled test chamber. (b) A snapshot of the arrangement of 18 alumina particles prior to projection. The reference particle is secured on the lower electrode using a small piece of double-sided adhesive tape. Due to the highly polished electrode surface, the images of the alumina particles are patent in the captured image. The diameter of the reference particle is 2.25 mm, measured using a caliper. (c) When a voltage is applied to the lower electrode, the particles acquire an electric charge and are projected. (d) Multiple forces act on a particle sitting on the electrode. These forces include its weight ($W = \text{mg}$) but also the Coulomb (F_c), image (F_{im}), and dipole (F_d) forces that comprise the total electrostatic force in Eq. (2). When the particle is in flight, the image and dipole forces become small and only the Coulomb force remains (see Fig. 2).

III. EXPERIMENTAL SETUP AND PROCEDURE

A. Experimental setup

Figure 3(a) shows the experimental setup used in this study, in which an electrostatic-particle-projection setup is located inside an environmentally controlled test chamber and is accessible through the door of the chamber [not shown in Fig. 3(a)]. The electrostatic-particle-projection setup is similar to that illustrated in Fig. 3(c), with an upper and a lower electrode having a disk shape. The lower electrode is fixed but the upper electrode with its attached adhesive layer is detachable and can be easily taken out through the door of the chamber. To minimize the risk of sparking between the edges of the two electrodes, especially at high electric field intensities, close to the dielectric breakdown of air, we choose an adhesive layer, attached to the upper electrode, to be disk shaped and slightly larger than the top electrode's surface, to fully cover the edges of the upper electrode. The lower and upper electrodes of the projection setup are, respectively, connected to $+V$ and ground terminals of a high-voltage power supply. The high-voltage power supply is from Trek® (Model 30/20 [61]) and is configured to provide dc voltages up to ± 30 kV. The environmentally controlled test chamber is equipped with an RH controller and a temperature controller, both from Electro-Tech Systems (ETS, model 5100 [62]). A general-purpose oscilloscope is used to monitor the voltage waveforms of the high-voltage power supply. Alumina particles (beads), with a nominal size of 500 μm, a standard deviation of 40 μm, and consisting of 99.5% alumina, are randomly picked from a batch purchased from Norstone®, Inc. [63]. A reference particle is randomly picked from a different batch of alumina particles from the same vendor, with a nominal size of 2 mm. As denoted in Fig. 3(b), the actual size of the reference particle is measured at 2.25 mm, using a caliper.

Particle size plays a pivotal role in the acquired particle-charge and projection parameters. To determine the precise size of the particles, we take photographs of them before projection and determine their size by comparing with the known size of the reference particle via image-analysis software. We take images of the arrangement of alumina particles adjacent to the reference particle using a Nikon D5200 high-resolution camera with an exposure time of 1/60 s, a focal length of 80 mm, an International Organization for Standardization (ISO) sensitivity of 100, and a focal ratio of F9. We adjust the ISO sensitivity to its lowest value to minimize the noise. Images of the arrangement of alumina particles are taken to determine the precise size of individual particles, using the FIJI software. An example of one of the still images is shown in Fig. 3(b), where 18 alumina particles are distributed in a single row. The reference particle is secured to the lower electrode's surface throughout the experiments using double-sided tape.

We record the projection of alumina particles using a high-speed video camera from Edgertronic [64], with a recording rate of 2000 frames/s. The high-speed video camera is coupled to the high-voltage power supply via a relay; as soon as the high-voltage power supply is turned on and an electric field is applied, the high-speed video camera starts to record a video of the projection of particles, if any. In this study, the window of application of

the electric field and the video recording of the particle projection is set to be 5 s throughout the experiments. We then analyze the captured videos using the ProAnalyst® motion-analysis software [65], which allows us to import the captured videos and then extract and quantify the motion of the projected particles within those videos. The transparent walls of the environmentally controlled test chamber are all completely sealed, except for a small hole for accommodating two cables, connecting the electrodes to the high-voltage power supply. Furthermore, the transparent walls of the environmentally controlled test chamber allow us to record images or videos of particles without any obstruction.

B. Experimental procedure

Before we distribute alumina particles on the lower electrode's surface, the lower electrode's surface is thoroughly and delicately cleaned using Kimwipes® wipers and isopropanol to remove any debris and oxidation from the metallic surface of the lower electrode. We prefer to use a chemical cleaner in lieu of an abrasive cleaning method to avoid changing the morphology and surface roughness of the lower electrode's surface. After securing the reference particle on the lower electrode's surface, we meticulously distribute 18 alumina particles in one straight line adjacent to the reference particle, equidistant from each other, using a fine pair of tweezers. We assign numbers to the distributed particles, where the leftmost particle in the aligned row is 1 and the rightmost particle, adjacent to the reference particle, is 18. Care is taken not to break or distort the alumina particles in transporting them from their corresponding batch to the top of the lower electrode's surface using the pair of tweezers. We then monitor the particles from the visor of the high-resolution camera to ensure that the particles are detectable within the frame and take an image of the arrangement of particles. Since the two cameras share the same view of the particles, we move the high-resolution camera to the side to clear the view for the high-speed video camera. We then set an RH level of the chamber using the RH controller at a desired level, close the door of the chamber, and wait for 5 min for the RH level to become stabilized. After stabilization of the RH level, we turn on the high-voltage power supply for only 5 s and the high-speed video camera records the projection of particles, if any. After the 5-s window, we turn off the high-voltage power supply, open the door of the chamber, remove particles that remain on the lower electrode's surface (not projected), detach the upper electrode and its attached adhesive layer, remove stuck particles from the adhesive layer using the pair of tweezers, and place the upper electrode back in the chamber.

We run the projection experiments for six RH levels and seven applied voltages. We repeat the above procedure twice, for a total of 36 particles, for every RH level and every applied voltage listed in Table I, which lists the RH levels used in this study as well as the nominal applied voltages and the actual applied voltages. The nominal-applied-voltage values denote the desired electric potential between the two electrodes set via the high-voltage power supply. However, due to some voltage reduction in the intervening circuitry, the actual electric potential established between the two electrodes, monitored on the oscilloscope's display, is different from the nominal values. Although the results in the next section are presented according to the nominal-voltage values, see Table I for the actual voltage values. We perform all the calculations, including the electric field intensity, the projection of the particles, and the motion analysis, using the actual voltage values. The numerical values of the parameters that we use in the calculations of this study are also listed in Table II.

TABLE I. The RH levels, nominal applied voltages, and actual applied voltages used in this study.

RH level (%)	30	40	50	60		70	80
Nominal applied voltage (kV)	12	15	18	21	24	27	30
Actual applied voltage (kV)	10.2	13.2	15.6	18	21	24	26.4

In the next section, we analyze the experimental results obtained in this study with the above-mentioned details. Note that the presented results, e.g., the average projection rate at different RH levels (see Fig. 4), may not necessarily be predictive of an industrial-scale process of electrostatic projection. In the latter case, excessive amount of particles (also known as abrasive grains) are fed onto a conveyor belt that goes through a region in which a high-intensity electric field with alternating polarity is applied. Further, in the industrial electrostatic projection, the projected particles form a "blizzard," i.e., by colliding with each other when traversing the air gap, and may experience multiple unsuccessful attempts to finally lodge in the adhesive layer. In this study, however, we intentionally place particles in one single row and maintain an interparticle distance above a minimum threshold level to circumvent having and then analyzing the very complex behavior of colliding particles. Analysis of the phenomenon of colliding

TABLE II. The parameters and constants used in this study.

Parameter	Numerical value
Relative permittivity of alumina, ε_p	10
Permittivity of free space, ε_0	8.85×10^{-12} F/m
Gravity, g	9.8 m/s^2
Dynamic viscosity of air at 25 °C, μ	1.84×10^{-5} Ns/m^2
Density of alumina, ρ_m	3950 kg/m^3
Thickness of adhesive layer, d	1.1 mm
Air gap, H	11.6 mm

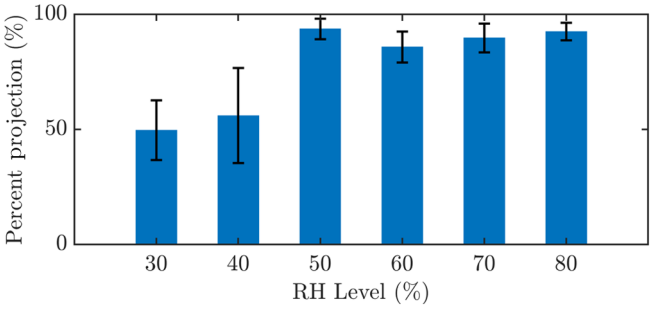

FIG. 4. The projection rate versus different RH levels. At each RH level, the average value is reported across all applied voltages and the error bar represents one standard deviation.

particles in an electrostatic projection process necessitates comprehensive studies and is beyond the scope of this investigation.

IV. RESULTS AND DISCUSSION

A. Projection rate

Figure 4 shows the average projection rate, defined as the percentage of the total number of projected particles for each RH level. Averaging is performed across all applied voltages. At 30% and 40% RH levels, the average projection rate is approximately 50% but it rises to more than approximately 85% as the RH level increases to 50% and higher. At each RH level, the error bar in Fig. 4 represents one standard deviation in the average projection rate across all applied voltages. At a 50% RH level and above, the average projection rate increases while the standard deviation decreases, which suggests that humidity plays a key role in the charge-transfer mechanism. We comment further on this hypothesis in Sec. IV E, where we discuss the projection time.

B. Particle size distribution

Figure 5 shows the particle size distribution of more than 1500 particles used in this study, whether projected or not, where their sizes are determined via the said procedure in the FIJI software. In addition, Fig. 5 shows a log-normal distribution curve that is fitted to the size distribution. The actual size of the analyzed alumina particles, with a nominal size of 500 μm, is between 380 μm and 650 μm, with a mean size of 495 μm and a standard deviation of 35 μm. According to the data sheet provided by the vendor, the mean size and standard deviation of the alumina particles are 537 μm and 41 μm, respectively.

C. Particle trajectory

Figure 6(a) illustrates individual trajectories for 1089 particles under different experimental conditions. Notably, increasing the electrode potential substantially decreases

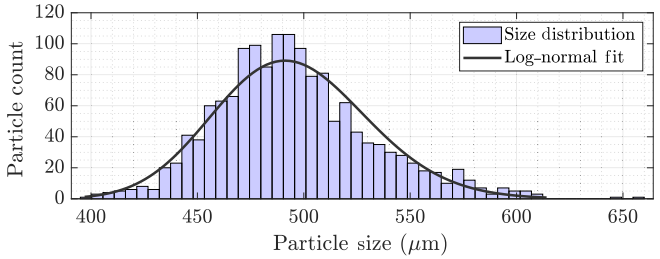

FIG. 5. The particle size distribution of all the particles used in this study, whether they are projected in the projection process or not, as well as the fitted log-normal distribution curve.

the flight time at any given RH. This is simply because Coulomb repulsion is stronger at higher electric field intensities. To analyze the data, we fit the parabolic trajectory, $y(t) = (QE - \mathrm{mg})t^2/2m$, to individual particle flight data and to estimate the total charge Q. Figure 6(b) illustrates the collapse of more than 98% of all trajectories to within 2% accuracy. More specifically, we accept the fitted value based on the following root-mean-square error (RMSE) criterion:

$$\sqrt{\frac{\sum_{i=1}^{N}(\tilde{y}_i - \tilde{t}_i^2)^2}{N}} < 0.02. \tag{10}$$

Here, $\tilde{y} = y/H$ is the normalized particle height based on the air gap H, $\tilde{t} = t/\sqrt{2H/a}$ is the normalized flight time, and $a = (QE - W)/m$ is the particle acceleration. For each trajectory, N is the number of frames captured by the high-speed video camera during the particle flight. Only 21 trajectories (out of 1089) fall outside this fitting criteria and their individual trajectories are shown in the inset of Fig. 6(b). The collapse of 1068 individual trajectories onto the parabolic trajectory, $\tilde{y} = \tilde{t}^2$, nicely illustrates that the drag force can safely be ignored in our analysis.

D. Particle charge

Figure 7 shows a scatter plot of the computed charge on individual particles and the solid line shows the best fit to the data. At 40% and higher RH levels, the charge scales with the particle size according to $Q \sim D^{2.2\pm0.2}$. This scaling suggests that most of the charge is stored on the surface of the particle. The data for a 30% RH level show a different scaling, albeit with greater uncertainty, $Q \sim D^{1.0\pm0.9}$. The large uncertainty could, in part, be due to the relatively narrow particle size distribution (see Fig. 5). More accurate characterization of the scaling exponent requires dedicated experiments with particles from a considerably wider size distribution.

Curiously, our experiments at the 30% RH level show consistently larger charge. This is better illustrated in Fig. 8, which illustrates the particle charge normalized by the saturation charge from Eq. (1) as a function of the

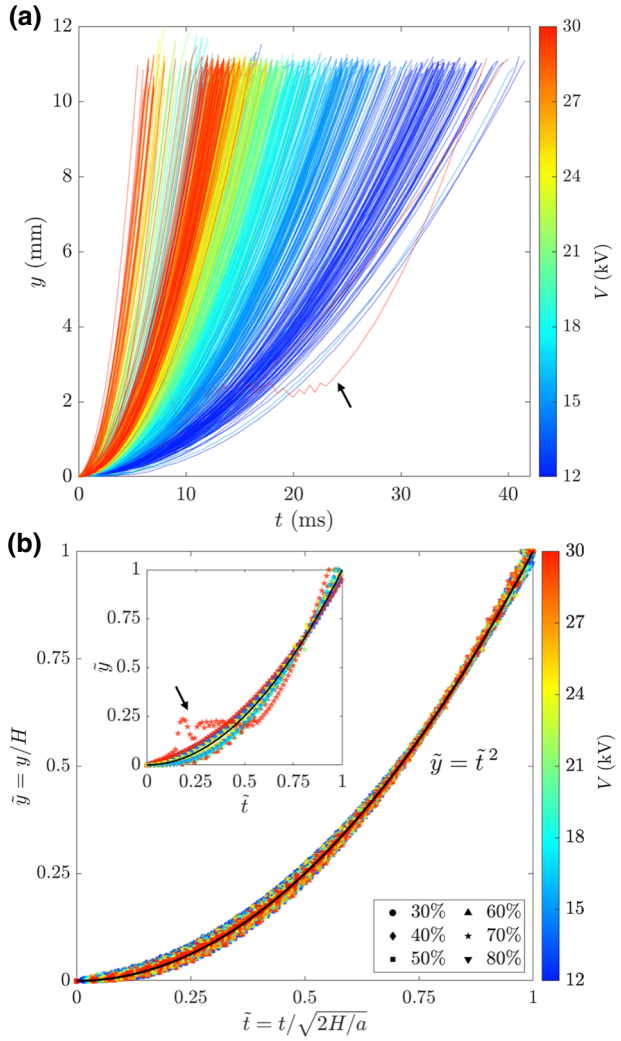

FIG. 6. Particle trajectories for different experimental conditions. (a) The individual trajectories indicate a strong dependence of the flight time on the applied field. (b) More than 98% of all trajectories fall within 2% of the parabolic trajectory, as demonstrated by the collapse of data in the rescaled coordinate. Here, H is the air gap between the two plates and $a = (QE - W)/m$ is the particle acceleration. The inset shows the few trajectories that fall outside of the 2% criterion (21 out of 1089). The peculiar trajectory (marked by the black arrow) is due to a collision between a particle and the reference particle during one of the experiments. Our software is not able to correctly extract the flight path for this particle.

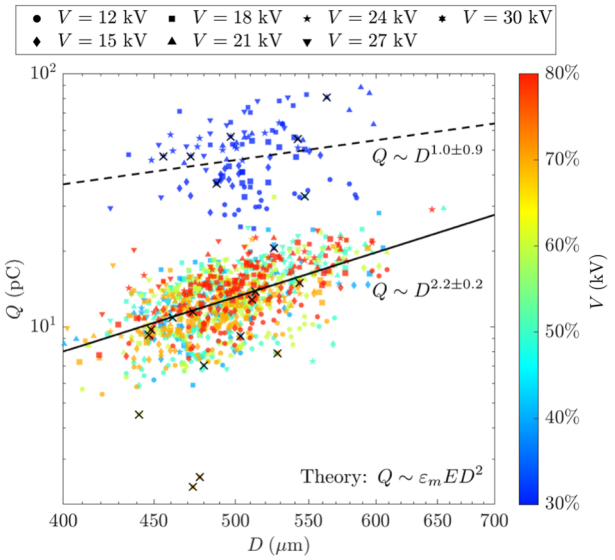

FIG. 7. The computed particle charge. The symbols represent different experimental conditions, while the crossed-out markers correspond to trajectories that do not satisfy the fitting condition in Eq. (10). Despite considerable spread, the data at 40% RH and above are consistent with a surface-charging mechanism ($Q \sim D^{2.2\pm0.2}$). The data at 30% RH show a considerably larger particle charge and a wider spread, as reflected by the uncertainty of the fitting exponent ($Q \sim D^{1.0\pm0.9}$).

applied electric field. The shaded area shows the set of all $(\tilde{E}, \tilde{Q})$ for which Eq. (4) is satisfied and projection is possible. The data for 40% RH and above generally follow the projection boundary given via Eq. (7). The overcharging ($Q > Q_{\min}$) might be due to unaccounted adhesive forces, e.g., capillary or particle-image interactions with adjacent particles [22]. Any such unaccounted adhesive force will maintain particle-electrode contact for a longer period of time and will allow for more charge transfer. The data at 30% RH show considerably larger charge than the saturation charge ($Q > Q_s$) as well as the data from the rest of the experiments. The cause of this anomaly is not clear to us. One possible hypothesis, yet untested, is that particles might have acquired static charge prior to the experiment. Nevertheless, we note that the particle trajectory at 30% RH collapses nicely onto the parabolic trajectory in Fig. 6(b). In fact, the deviation from the parabolic trajectory at 30% RH is no more than for other experiments at higher RH levels, which suggests similar confidence in the computed particle charge.

E. Projection time

In this section, we analyze the particle projection time. Our experiments are conducted under a dc electric field. However, in an industrial plant, electrostatic projection is usually performed using an ac electric field and knowledge of the projection time could help determine the operating frequency. The reason for using an ac field during the industrial process is to neutralize the electric charge that is accumulated on the conveyor belt (see Fig. 1) during charging of particles. Because the conveyor belt is electrically insulating, this accumulated charge would not dissipate under a dc field and it would eventually reduce the effective electric field felt by the particles. In our current setup, we place the particles directly on top of a bare metal electrode, which does not suffer from this limitation. This allows us to perform the experiments under a dc field. Nevertheless, analysis of the projection time reveals

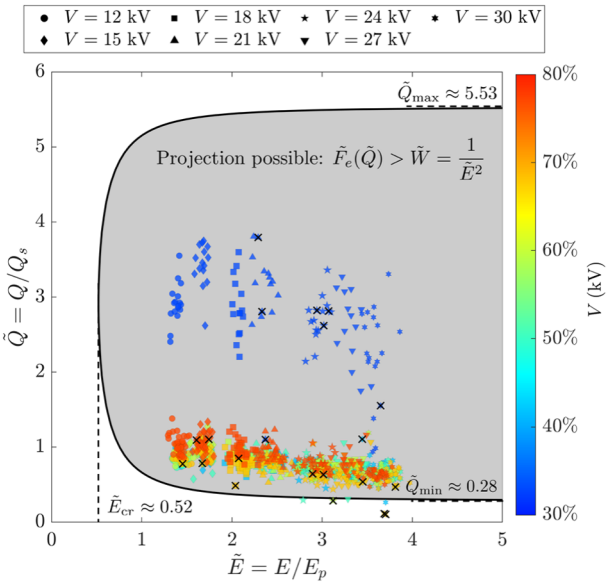

FIG. 8. The computed normalized charge versus the applied electric field for individual particles. The crossed-out markers correspond to trajectories that do not satisfy the fitting condition in Eq. (10). The shaded area illustrates the set of all $(\tilde{E}, \tilde{Q})$ values for which projection is possible, since the electrostatic force is strong enough to overcome the weight of the particle [see Eq. (4)]. The computed charge for all but six (>99%) of the particles falls within the projection region. The data at 30% RH show a considerably larger charge than the saturation value ($Q > Q_s$), possibly due to triboelectric charging. At 40% and higher RH, the normalized particle charge decreases with an increase in the electric field, consistent with the minimum required charge predicted by Eq. (7).

valuable information about the charge-transfer mechanism and electrostatic projection.

We express the projection time as the sum of two contributions. First, once the electric field is applied, particles must acquire enough charge for Coulomb repulsion to overcome gravity, and possibly other attractive forces, and levitate. We refer to this timing as the "lift-off time" and denote it by t_l. Second, the particles must traverse the air gap between the two electrodes before the polarity of the field can be switched (in the case of an ac field). We refer to this timing as the "flight time" and denote it by t_f. The projection time is therefore written as $t_p = t_l + t_f$.

1. Flight time

The particle flight time is well described by the balance between Coulomb repulsion and gravity. This is evident in the collapse of the trajectory data in Fig. 6(b), which suggests that

$$t_f = \sqrt{\frac{2Hm}{QE - W}}, \tag{11}$$

where m is the particle mass and $W = mg$ is its weight. Figure 9(a) clearly illustrates that the flight time for virtually all particles is accurately described by Eq. (11). Figure 9(b) illustrates the inverse scaling of the flight time with the applied voltage, i.e., $t_f \sim 1/V$. This scaling directly results from Eq. (11) where, to leading order, the weight of the particle can be ignored compared to the Coulomb repulsion [cf. Fig. 9(b)].

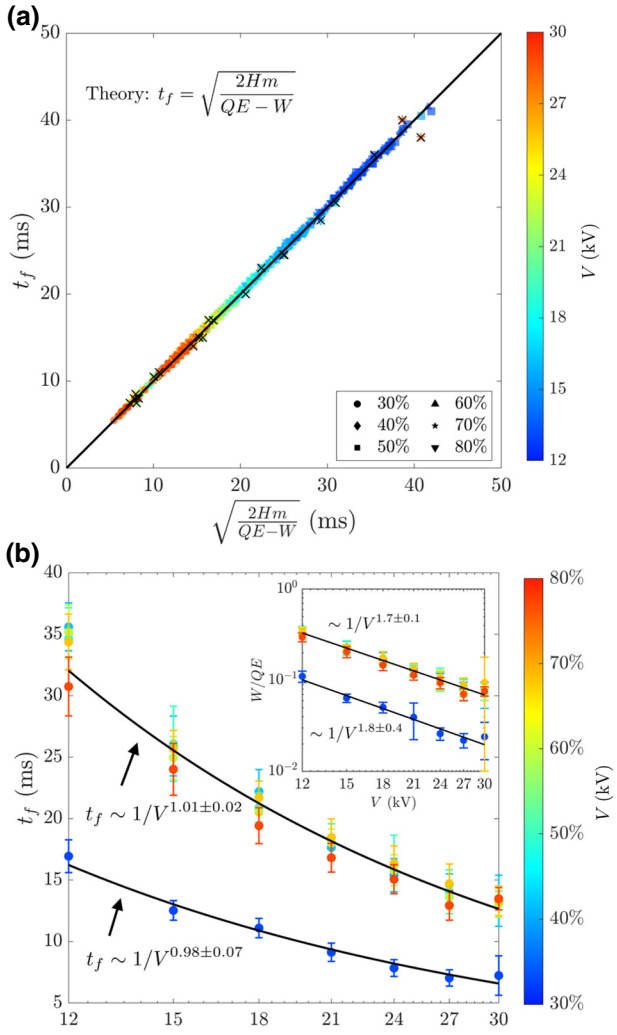

FIG. 9. The particle flight time is accurately described by the balance between Coulomb repulsion and gravity. (a) We plot the measured flight time (t_f) versus the predicted value from Eq. (11). Our measurements agree well with the prediction, as suggested by the collapse of the data on the diagonal line. (b) The average value of the flight time for different experiments, where the error bar indicates one standard deviation. The flight time scales inversely with the applied potential and only weakly depends on the humidity level at 40% RH and above. This results directly from the linear scaling of the particle charge with the electric field and the fact that the Coulomb force is considerably stronger than gravity (see inset). The flight time at 30% RH is noticeably shorter due to the higher electric charge acquired by the particles (cf. Fig. 7).

2. Lift-off time

Figure 10(a) illustrates variation of the lift-off time, i.e., the time it takes for particles to acquire enough charge and levitate after the electric field is applied. The lift-off time is nearly constant below the 40% RH level and decreases dramatically by going to higher RH levels. The solid line in Fig. 10(a) is an empirical exponential fit to the data,

$$t_l \approx \tau_0 e^{-15(h-h_0)}, \quad h \geq h_0, \tag{12}$$

where $h = P_v/P_{\text{sat}}$ is the RH, $\tau_0 \approx 2.4$ (s), and $h_0 = 0.4$ is the threshold humidity at which we first observe a decrease in the lift-off time. The charging process may be understood in terms of an equivalent RC circuit, i.e., $Q(t) = Q_s[1 - \exp(-t/\tau)]$ [see Fig. 10(b)]. Here, $\tau = R_{\text{eff}}C_p$ is the characteristic RC time scale, written in terms of the particle capacitance (C_p) and an effective charge-transfer resistance (R_{eff}) between the particle and the electrode. The particle capacitance may be estimated from the saturation charge [Eq. (1)] as $C_p = Q_s/V \sim \varepsilon_m R \sim 10^{-15}$ F, where $V \sim RE$ is the potential difference between the particle and its image. By measuring the lift-off time, it is possible to estimate the effective resistance between the particle and the electrode via

$$R_{\text{eff}} \approx \frac{t_l}{C_p} \approx R_0 e^{-15(h-h_0)}, \quad h \geq h_0, \tag{13}$$

where $R_0 \approx 2.4 \times 10^{15}$ Ω. The effective resistance is comprised of two contributions, i.e., $R_{\text{eff}} = R_p + R_c$, where $R_p \sim \rho_p/R$ is the particle resistance with an effective bulk resistivity ρ_p and R_c is the contact resistance between the particle and the electrode. The electrical resistivity of single-crystal alumina is very high, at $\rho_p \sim 10^{15}$ Ω cm [66], and corresponds to a particle resistance of roughly $R_p \sim 4 \times 10^{16}$ Ω, which is much larger than the inferred effective resistance. Indeed, the effective resistance value at an 80% RH level suggests that the effective particle resistivity cannot be more than $\rho_p \approx 2.5 \times 10^{10}$ Ω cm and that the charge transfer is likely limited by the contact resistance. This value is consistent with our own independent dielectric spectroscopy measurements, which yield $\rho_p \approx 2.5 \times 10^{9}$ Ω cm at a 50% RH level (data not shown), by fitting the permittivity and loss tangent for a packed bed of alumina balls (2–5 mm thick at 67% volume fraction) pressed in a cup between two electrodes (20 mm in diameter).

To explain the dependence of the resistance on the RH level, it is necessary to understand the charge-transfer mechanism between an insulator particle and a metal electrode. However, this is a debated topic [67] with competing hypotheses involving both ion- and electron-transfer processes [68,69]. One possibility is that charge transfer is primarily due to electromigration of ions, either protons (H^+) or hydroxyl ions (OH^-), to and from the particle. A variant of this hypothesis, based on asymmetric partitioning and adsorption of hydroxide ions [69], has recently been used to explain contact electrification between insulating surfaces with electric fields [70,71].

This ionic picture of charge transfer necessitates the presence of water, both at a contact point of the particle

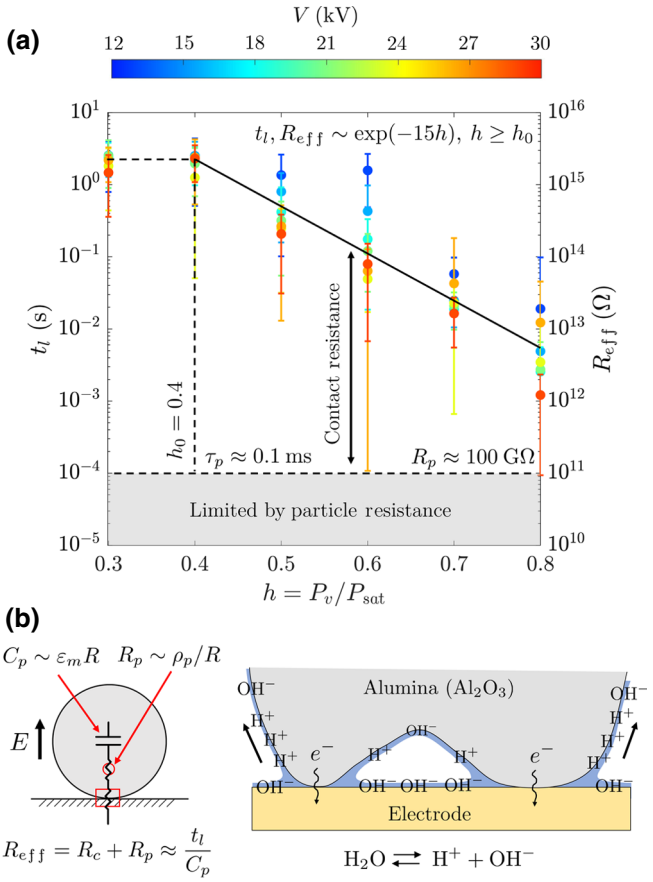

FIG. 10. The effect of the RH on the lift-off time and charge transfer. (a) The lift-off time is nearly constant below a 40% RH level ($h_0 = 0.4$) but decreases dramatically above h_0. The symbols represent the average value during each experiment and the error bar indicates one standard deviation. The solid line represents the best exponential fit to the data. The effective resistance, $R_{\text{eff}} = R_p + R_c$, is estimated from the lift-off time, t_l, and the particle capacitance, C_p, i.e., $R_{\text{eff}} \approx t_l/C_p$. The horizontal dashed line indicates charge-transfer limitation by the particle based on the estimated effective particle resistivity of $\rho_p \sim 10^9$ Ω cm, obtained via independent dielectric spectroscopy measurements at 50% RH (data not shown). (b) The charging mechanism can be understood in terms of an equivalent RC circuit. The particle capacitance may be estimated from the saturation charge [see Eq. (1)]. The effective resistance is the sum of two contributions: the particle resistance ($R_p \sim \rho_p/R$) and the contact resistance between the particle and the electrode (R_c). The particle resistance might be interpreted as either the bulk resistance or the surface resistance, depending on whether the charge transfer is dominated by ion- (H^+ and OH^-) or electron-transfer processes.

and the electrode as well as on the particle surface. At high enough RH levels, this is feasible through adsorption of molecularly thin water films on the particle surface and nucleation of "water bridges" through capillary condensation at the contact point [72,73]. Both effects are amplified at higher RH levels and increase the rate of charge transfer, thereby reducing the effective resistance. In particular, the surface resistance may be estimated as $R_s \sim \rho_w/\lambda$, where ρ_w is the water resistivity and λ is the thickness of the adsorbed layer. For pure water, $\rho_w \sim 10^7\ \Omega\,\mathrm{cm}$ and $\lambda \sim 0.5$ nm, the surface resistance is roughly $R_s \sim 10^{14}\ \Omega$. Note that adsorption of CO_2 from the surrounding air can increase the water conductivity and further lower the surface resistance, possibly down to $R_s \sim 10^{13}\ \Omega$. This simple estimation assumes that the surface water forms a percolating pathway, which is only possible above a certain RH level. This might be related to the threshold RH level of 40% that we experimentally observe in Fig. 10. We caution, however, that further detailed experiments, possibly guided by surface characterization, are required to definitively test this hypothesis. Nevertheless, we note that many metal oxides exhibit similarly enhanced electrical conductivity at high RH levels and are routinely used as humidity sensors in the form of porous ceramics [74–80].

Alternatively, charge transfer might also occur due to electron transfer between alumina particles and the electrode at direct contact points [see Fig. 10(b)]. Indeed, solid-solid electron transfer has recently been implicated as a rate-determining step in the similar situation of Li-ion-battery cathodes, albeit at lower electric fields, where electrons slowly transfer from a conducting carbon coating or an additive to transition-metal sites in an insulating solid material (such as iron phosphate) as it intercalates lithium ions [81], consistent with the predictions of the Marcus theory [82,83]. Here, electron transfer from surface oxygen atoms could be an inner-sphere process [84], in which adsorbed water molecules near the contact point facilitate adiabatic electron transfer by strengthening the electronic coupling. Moreover, the increased local permittivity from adsorbed moisture would amplify the local electric field around the contact point, thus further enhancing the probability of electron transfer at high voltage.

V. CONCLUSION

In this paper, we study the electrostatic projection of spherical alumina particles in different RH conditions and electric field intensities by using a high-speed video imaging setup. We present a simple theory for computing the minimum required electric field and particle charge that is needed for projection. We also give a simple expression for the particle trajectory, which we use to infer the particle charge by analyzing the high-speed video images. Throughout this analysis, we note that the drag force is justifiably negligible, as the Coulomb repulsion is significantly stronger than the drag force and the projected particles essentially follow a parabolic trajectory. In addition, we observe that when the RH level is maintained at a particular level, increasing the electric field strength does not necessarily increase the projection rate. When the RH level is kept at 50% and above, the average projection rate is higher than 85%, independent of the applied electric field. Increasing the electric field intensity substantially decreases the flight time at any RH level, as Coulomb repulsion becomes stronger at higher electric field intensities. For particles projected at a 40% RH level and above, the amount of accumulated charge closely follows theoretical predictions. However, the particles at a 30% RH level are consistently charged more highly than the saturation value. One hypothesis, though untested, is that this anomaly might be due to preexisting triboelectric charging, which cannot be explained in our framework. These particles also have a considerably shorter flight time compared to particles at higher RH levels due to stronger Coulomb repulsion. Finally, we also observe a strong reduction of lift-off at the 40% RH level and above. We believe that this phenomenon could be due to the formation of thin water films at higher RH levels, which can significantly enhance the charge transfer and shorten the lift-off time. Nevertheless, further theoretical and experimental work is needed to establish a precise mechanism behind this accelerated charging phenomenon.

Our perspective on electrostatic projection as an extreme case of induced-charge electrokinetic phenomena [12,17] suggests that broken symmetries in the particle shape or surface properties [15,18,85–87], especially in collections of interacting particles [88–90], will lead to rich new physics. In particular, asymmetric grains can be expected to tilt and rotate during induction charging [18], just as asymmetric polarizable particles in liquid electrolytes have been observed to translate [20] and rotate [21] near surfaces [19] in uniform dc or ac fields. Orientation during induction charging and in flight will also be influenced by the presence of other nearby particles and surface heterogeneities, which affect charge transfer, polarization, local electric fields, and hydrodynamic interactions.

There are also important differences for electrostatic projection in air, however, related to the lack of surface-generated electro-osmotic flows and the much higher Reynolds number of gas flow. The latter can lead to persistent inertial rotation during flight, despite the aligning influence of the electric field, as well as to complex electrohydrodynamic interactions in realistic situations. In the manufacturing process for coated abrasives, the resin-coated web (projection target) also moves rapidly (>1 cm/s) with respect to the grain belt below it, separated by a thin air gap (<1 cm), and large groups of particles project and fall periodically in response to alternating high voltage, in some cases producing a swirling "blizzard"

of particles and agglomerates. It would be interesting to explore these highly nonlinear collective phenomena with high-speed video imaging in future works, building on this initial attempt to shed light on the physics of electrostatic projection for isolated spherical grains.

ACKNOWLEDGMENTS

We acknowledge the support from Saint-Gobain Research North America, Northborough, MA, for sponsoring this research project. M.M. acknowledges discussions with J. Pedro de Souza, Dimitrios Fraggedakis, Tingtao Zhou, and Michael P. McEldrew. We also acknowledge the contributions from our colleagues in Saint-Gobain Research North America, especially Sid Wijesooriya for providing imaging equipment.

A.S. and M.M. contributed equally to this work.

APPENDIX: NONIDEAL BEHAVIOR OF PROJECTED PARTICLES

In our projection experiments, a small fraction of the particles do not follow the ideal behavior of acquiring electric charge, overcoming attractive forces, leaving the lower electrode's surface, traversing the air gap along a straight line, hitting the adhesive layer, and sticking to it. In analyzing the projection videos, we categorize these occasional forms of nonideal behavior into two groups.

1. 2D flight trajectory

As discussed in Sec. II, we assume that the projected particles move along a straight line in the y direction. In extracting flight data from the videos, we take into consideration movement of projected particles in only the y direction and ignore displacement of particles along the x axis, if they have any. As clearly addressed in the presentation of the flight trajectories in Sec. IV C, some of the flight trajectories do not collapse onto the general flight trajectory. The reason, in part, is attributable to the fact that their flight trajectories have a displacement in the x direction along their path toward the adhesive layer but this displacement is not considered in the analysis. Indeed, the aforesaid projected particles deviate from the straight line along the y axis and instead follow a curved path when their distance from their neighboring particles, either still in contact with the lower electrode's surface or close to projection, is less than a particular threshold. Figure 11 illustrates the flight trajectories of some of the particles throughout the experiment and is representative of all the nonidealities in the current study in which projected particles do not follow the straight line. We extract individual frames from the recorded projection videos using MATLAB®, select a number of frames that show nonideal behavior of the targeted particle(s) in the course of projection, and stack the selected frames using StarStaXcopyright [91]. In Figs. 11(a)–11(d), our focus is on the projection of particle 18, the rightmost particle in the

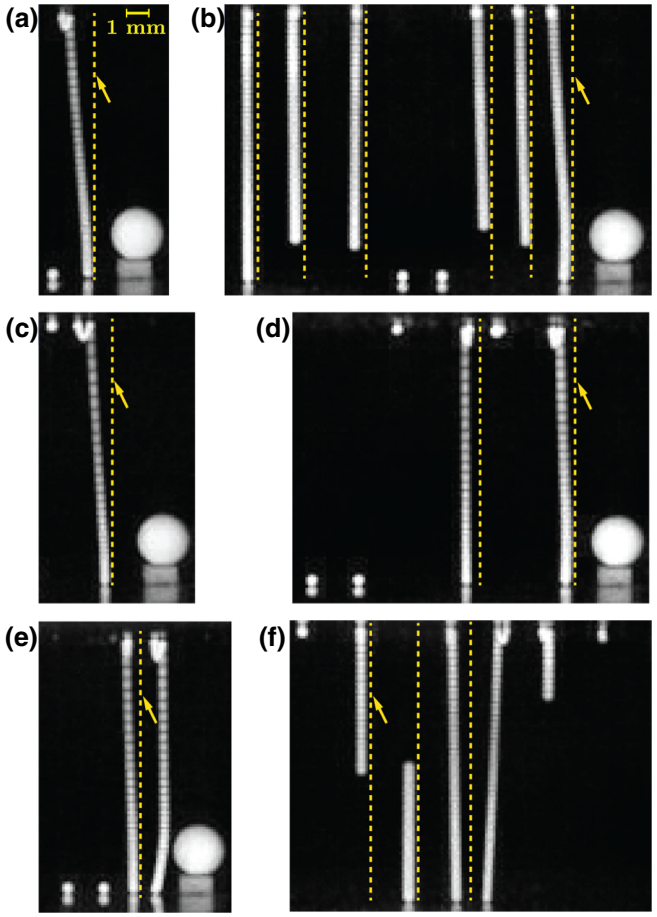

FIG. 11. Stacked frames of the projection of particles and their deviation from a hypothetical straight line, clarified by an arrow, along the y axis. (a) The first round of projections at the 40% RH level and 18 kV applied voltage, where particle 17 is still in contact with the lower electrode's surface while particle 18 deviates from the straight line. (b) The first round of projections at the 70% RH level and 12 kV applied voltage, where particles 11, 12, and 13 closely follow the straight line and particles 14 and 15 are still in contact with the lower electrode's surface, while the flight trajectories of particles 16, 17, and 18 deviate from the straight line—particle 18 experiences the most significant deviation. (c) The first round of projections at 40% RH and 21 kV applied voltage, where the flight trajectory of particle 18 deviates from the straight line and particle 17 is already attached to the adhesive layer. (d) The first round of projections at 50% RH and 21 kV applied voltage, where particles 13 and 14 are still in contact with the lower electrode's surface, particles 15 and 17 are already attached to the adhesive layer, and the flight trajectory of particle 16 is closely following the straight line, while the flight trajectory of particle 18 is deviating from the straight line. (e) The first round of projections at 60% RH and 21 kV applied voltage, where particles 15 and 16 are still in contact with the lower electrode's surface, while the flight trajectories of particles 17 and 18 are deviating from the straight line. (f) The first round of projections at the 70% RH level and 12 kV, where particles 1 (the leftmost) and 7 (the rightmost) are attached to the adhesive layer, particles 2, 3, and 6 are still in flight to reach the adhesive layer and follow the straight line, while the flight trajectory of particle 5 is deviating from the straight line.

arrangement of 18 distributed particles and adjacent to the reference particle. In Figs. 11(a)–11(d), particle 18 does not traverse the air gap along the straight line once projected. Instead, particle 18 experiences a deflection from the straight line once it detaches from the lower electrode's surface and traverses the air gap along a curved path. It is to be noted that both the reference particle and particle 18 acquire positive electric charge. Hence, a relatively strong local electric field, stemming from the reference particle, is repelling particle 18 and causing the deflection from the straight line. The relatively strong local electric field of the reference particle is attributable to its size, which is approximately four times than that of particle 18.

We observe deflections from the straight line from other particles as well. Figure 11(e) shows the projections of particles 17 and 18, where both particles project almost simultaneously and experience deflections from the straight line in initial time instants of their flight. Repelled by particle 17, particle 18 moves toward the reference particle; subsequently repelled by the reference particle, it follows a path parallel to the straight line that is shown. In Fig. 11(f), the behavior of the first seven distributed particles has been examined (numbered from the left to the right). While particle 4 follows the straight line reasonably well, particle 5, affected by particle 4, follows the curved path. The flight trajectories of particles 2, 3, and 6, though partially shown due to the selected frames, are along the straight line. Particles 1 and 7 have been attached to the adhesive layer before the first selected frame. As is understood from Fig. 11(f), the deviation of the flight trajectory of particle 5 from the straight line is attributed to two factors: (1) the distance between adjacent particles 4 and 5 is less than a particular threshold; and (2) the lift-off times of particles 4 and 5 are substantially close at 62 and 65 ms, respectively. Therefore, their distance in initial time instants of the projection remains almost unchanged until the interparticle repelling force causes the deflection in the flight trajectory of particle 5. On the contrary, the flight trajectories of particles 2 and 3 in Fig. 11(f) are not affected by each other, as their relative distance is more than the distance between particles 4 and 5. In addition, with 38 and 87 ms as the lift-off times for particles 2 and 3, respectively, their flight trajectories are not impacted by any particle in their proximity. Similarly, the relative distance between particles 3 and 4 is more than the distance between particles 4 and 5 and particle 4 has traversed almost half of the air gap when particle 3 leaves the lower electrode's surface.

2. Projection at high RH levels

We observe peculiar forms of behavior from some of the particles at the 70% and 80% RH levels, where projected particles hit the adhesive layer, adhere to the adhesive layer for an infinitesimal amount of time, lose their charge, fall off on the lower electrode's surface, regain charge, project again, and finally adhere to the adhesive layer. Throughout analyzing the recorded videos, we observe the most

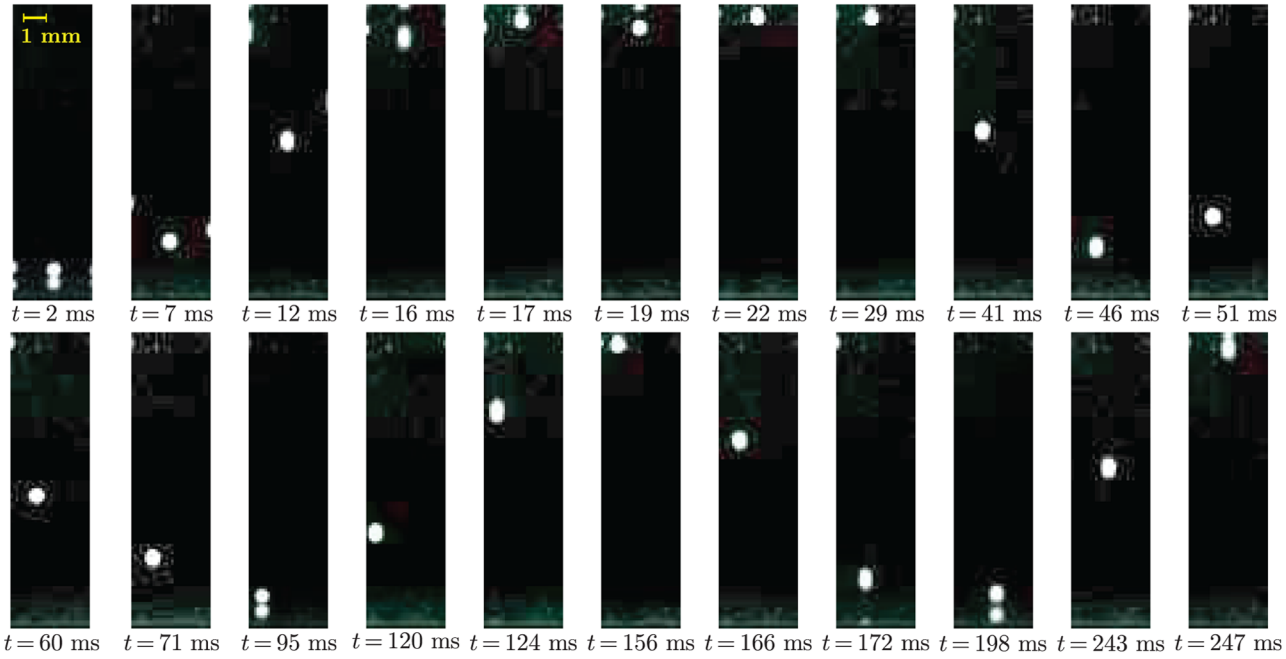

FIG. 12. The peculiar behavior of particle 7 in the second round of projections at the 80% RH level and 27 kV applied voltage in the 5-s window during which the voltage is applied. Particle 7 hits the adhesive layer and returns to the lower electrode's surface twice before finally lodging in the adhesive layer at $t = 247$ ms.

notable behavior for particle 7 in the second round of projections at the 80% RH level and 27 kV applied voltage. Figure 12 illustrates 22 snapshots of the behavior of particle 7 at different time instants, where particle 7 adheres to the adhesive layer twice for very short periods of time before finally lodging in it. It is to be noted that despite the fact that particle 7 does not adhere completely to the adhesive layer the first time it hits the adhesive layer, we consider the first lift-off time and the first flight time in the analysis presented above.

When particle 7 departs the lower electrode's surface within 2 ms of applying the electric field and hits the adhesive layer with a very high momentum, it bounces back and forth on the adhesive layer. Particle 7 loses at least a portion of its acquired charge in this back-and-forth motion, until it adheres to the adhesive layer for 6 ms. It then falls off onto the lower electrode's surface. After bouncing back and forth on the lower electrode's surface, it acquires charge again within 3.5 ms, i.e., a second lift-off time, and moves toward the adhesive layer. After a loose adhesion to the adhesive layer that lasts for 22 ms, the particle falls off and comes into contact with the lower electrode's surface, gains charge within 2.5 ms, i.e., a third lift-off time, and moves toward the adhesive layer to finally lodge in it.

We speculate that condensation of thin water films around the particle and on the adhesive layer, both due to high RH level, might contribute to the loose adherence between the particle and the adhesive layer. Another possibility is that particle 7, with a diameter of 0.57 mm (the largest amongst the 18 particles), might be hitting the adhesive layer with a high momentum, causing it to bounce back and attach loosely to the adhesive layer.

We also observe similar but less complex forms of behavior than the afore-mentioned types from some of the particles in the following three cases: (1) the first round of projections at the 70% RH level and 21 kV applied voltage; (2) the first round of projections at the 80% RH level and 24 kV applied voltage; and (3) the second round of projections at the 80% RH level and 27 kV applied voltage.

[1] W. B. Russel, D. A. Saville, and W. R. Schowalter, *Colloidal Dispersions* (Cambridge University Press, Cambridge, UK, 1991).

[2] J.-L. Viovy, Electrophoresis of DNA and other polyelectrolytes: Physical mechanisms, Rev. Mod. Phys. **72**, 813 (2000).

[3] K. D. Dorfman, DNA electrophoresis in microfabricated devices, Rev. Mod. Phys. **82**, 2903 (2010).

[4] O. O. Van der Biest and L. J. Vandeperre, Electrophoretic deposition of materials, Annu. Rev. Mater. Sci. **29**, 327 (1999).

[5] L. Besra and M. Liu, A review on fundamentals and applications of electrophoretic deposition (EPD), Prog. Mater. Sci. **52**, 1 (2007).

[6] J. B. Fenn, M. Mann, C. K. Meng, S. F. Wong, and C. M. Whitehouse, Electrospray ionization for mass spectrometry of large biomolecules, Science **246**, 64 (1989).

[7] M. S. Onses, E. Sutanto, P. M. Ferreira, A. G. Alleyne, and J. A. Rogers, Mechanisms, capabilities, and applications of high-resolution electrohydrodynamic jet printing, Small **11**, 4237 (2015).

[8] S. Mhatre, V. Vivacqua, M. Ghadiri, A. Abdullah, M. Al-Marri, A. Hassanpour, B. Hewakandamby, B. Azzopardi, and B. Kermani, Electrostatic phase separation: A review, Chem. Eng. Res. Des. **96**, 177 (2015).

[9] J. S. Eow, M. Ghadiri, A. O. Sharif, and T. J. Williams, Electrostatic enhancement of coalescence of water droplets in oil: A review of the current understanding, Chem. Eng. J. **84**, 173 (2001).

[10] F. Mugele and J.-C. Baret, Electrowetting: From basics to applications, J. Phys.: Condens. Matter **17**, R705 (2005).

[11] D. R. Link, E. Grasland-Mongrain, A. Duri, F. Sarrazin, Z. Cheng, G. Cristobal, M. Marquez, and D. A. Weitz, Electric control of droplets in microfluidic devices, Angew. Chem. Int. Ed. **45**, 2556 (2006).

[12] M. Z. Bazant and T. M. Squires, Induced-charge electrokinetic phenomena, Curr. Opin. Colloid Interface Sci. **15**, 203 (2010).

[13] N. Gamayunov, V. Murtsovkin, and A. Dukhin, Pair interaction of particles in electric field. 1. Features of hydrodynamic interaction of polarized particles, Colloid J. USSR (Engl. Transl.); (United States) **48**, 233 (1986).

[14] V. Murtsovkin, Nonlinear flows near polarized disperse particles, Colloid J. **58**, 341 (1996).

[15] M. Z. Bazant and T. M. Squires, Induced-Charge Electrokinetic Phenomena: Theory and Microfluidic Applications, Phys. Rev. Lett. **92**, 066101 (2004).

[16] T. M. Squires and M. Z. Bazant, Induced-charge electro-osmosis, J. Fluid Mech. **509**, 217 (2004).

[17] M. Z. Bazant, M. S. Kilic, B. D. Storey, and A. Ajdari, Towards an understanding of induced-charge electrokinetics at large applied voltages in concentrated solutions, Adv. Colloid Interface Sci. **152**, 48 (2009).

[18] T. M. Squires and M. Z. Bazant, Breaking symmetries in induced-charge electro-osmosis and electrophoresis, J. Fluid Mech. **560**, 65 (2006).

[19] M. S. Kilic and M. Z. Bazant, Induced-charge electrophoresis near a wall, Electrophoresis **32**, 614 (2011).

[20] S. Gangwal, O. J. Cayre, M. Z. Bazant, and O. D. Velev, Induced-Charge Electrophoresis of Metallodielectric Particles, Phys. Rev. Lett. **100**, 058302 (2008).

[21] A. Boymelgreen, G. Yossifon, S. Park, and T. Miloh, Spinning Janus doublets driven in uniform ac electric fields, Phys. Rev. E **89**, 011003 (2014).

[22] T. B. Jones, *Electromechanics of Particles* (Cambridge University Press, New York, NY, USA, 2005).

[23] P. Richetti, J. Prost, and P. Barois, Two-dimensional aggregation and crystallization of a colloidal suspension of latex spheres, J. De Physique Lettres **45**, 1137 (1984).

[24] M. Giersig and P. Mulvaney, Formation of ordered two-dimensional gold colloid lattices by electrophoretic deposition, J. Phys. Chem. **97**, 6334 (1993).

[25] M. Giersig and P. Mulvaney, Preparation of ordered colloid monolayers by electrophoretic deposition, Langmuir **9**, 3408 (1993).

[26] M. Böhmer, *In situ* observation of 2-dimensional clustering during electrophoretic deposition, Langmuir **12**, 5747 (1996).

[27] M. Trau, D. Saville, and I. A. Aksay, Field-induced layering of colloidal crystals, Science **272**, 706 (1996).

[28] M. Trau, D. Saville, and I. A. Aksay, Assembly of colloidal crystals at electrode interfaces, Langmuir **13**, 6375 (1997).

[29] R. Hayward, D. Saville, and I. A. Aksay, Electrophoretic assembly of colloidal crystals with optically tunable micropatterns, Nature **404**, 56 (2000).

[30] W. Ristenpart, I. A. Aksay, and D. Saville, Electrically Guided Assembly of Planar Superlattices in Binary Colloidal Suspensions, Phys. Rev. Lett. **90**, 128303 (2003).

[31] P. J. Sides, Electrohydrodynamic particle aggregation on an electrode driven by an alternating electric field normal to it, Langmuir **17**, 5791 (2001).

[32] W. Ristenpart, I. A. Aksay, and D. Saville, Assembly of colloidal aggregates by electrohydrodynamic flow: Kinetic experiments and scaling analysis, Phys. Rev. E **69**, 021405 (2004).

[33] D. C. Prieve, P. J. Sides, and C. L. Wirth, 2-D assembly of colloidal particles on a planar electrode, Curr. Opin. Colloid Interface Sci. **15**, 160 (2010).

[34] W. M. Winslow, Induced fibration of suspensions, J. Appl. Phys. **20**, 1137 (1949).

[35] A. P. Gast and C. F. Zukoski, Electrorheological fluids as colloidal suspensions, Adv. Colloid Interface Sci. **30**, 153 (1989).

[36] T. C. Halsey, Electrorheological fluids, Science **258**, 761 (1992).

[37] P. Sheng and W. Wen, Electrorheological fluids: Mechanisms, dynamics, and microfluidics applications, Annu. Rev. Fluid Mech. **44**, 143 (2012).

[38] Y.-M. Jung, H.-C. Oh, and I. S. Kang, Electrical charging of a conducting water droplet in a dielectric fluid on the electrode surface, J. Colloid Interface Sci. **322**, 617 (2008).

[39] D. J. Im, J. Noh, D. Moon, and I. S. Kang, Electrophoresis of a charged droplet in a dielectric liquid for droplet actuation, Anal. Chem. **83**, 5168 (2011).

[40] D. J. Im, M. M. Ahn, B. S. Yoo, D. Moon, D. W. Lee, and I. S. Kang, Discrete electrostatic charge transfer by the electrophoresis of a charged droplet in a dielectric liquid, Langmuir **28**, 11656 (2012).

[41] A. M. Drews, H.-Y. Lee, and K. J. Bishop, Ratcheted electrophoresis for rapid particle transport, Lab Chip **13**, 4295 (2013).

[42] A. M. Drews, C. A. Cartier, and K. J. Bishop, Contact charge electrophoresis: Experiment and theory, Langmuir **31**, 3808 (2015).

[43] G. Hartmann, L. Marks, and C. Yang, Physical models for photoactive pigment electrophotography, J. Appl. Phys. **47**, 5409 (1976).

[44] D. M. Pai and B. E. Springett, Physics of electrophotography, Rev. Mod. Phys. **65**, 163 (1993).

[45] E. Kelly and D. Spottiswood, The theory of electrostatic separations: A review part I. Fundamentals, Miner. Eng. **2**, 33 (1989); E. Kelly and D. Spottiswood, The theory of electrostatic separations: A review part II. Particle charging, Miner. Eng. **2**, 193 (1989); E. Kelly and D. Spottiswood, The theory of electrostatic separations: A review part III. The separation of particles, Miner. Eng. **2**, 337 (1989).

[46] R. P. Carlton, Manufacture of abrasives, U.S. Patent No. 2,370,636 A (March 6, 1945).

[47] E. M. Ransburg, Electrostatic coating apparatus, U.S. Patent No. US 2,684,656 A (July 27, 1954).

[48] W. J. McDonald, An analysis of electrostatic deposition of particulate solids, IEEE Trans. Ind. Appl. **IA-8**, 651 (1972).

[49] L. S. Moren, B. G. Koethe, and E. L. Thurber, Layered particle electrostatic deposition process for making a coated abrasive article, U.S. Patent No. US 8,551,577 B2 (October 8, 2013).

[50] Y. Wu, G. Castle, I. Inculet, S. Petigny, and G. Swei, Induction charge on freely levitating particles, Powder. Technol. **135–136**, 59 (2003).

[51] Y. Wu, G. S. P. Castle, I. I. Inculet, S. Petigny, and G. S. Swei, The effect of electric field strength on the induction charge of freely levitating particles, IEEE Trans. Ind. Appl. **40**, 1498 (2004).

[52] Y. Wu, G. S. P. Castle, and I. I. Inculet, Induction charging of granular materials in an electric field, IEEE Trans. Ind. Appl. **41**, 1350 (2005).

[53] Y. Wu, G. Castle, and I. Inculet, Particle size analysis in the study of induction charging of granular materials, J. Electrostat. **63**, 189 (2005).

[54] M. Sow, R. Widenor, A. R. Akande, K. S. Robinson, R. M. Sankarana, and D. J. Lacks, The role of humidity on the lift-off of particles in electric fields, J. Braz. Chem. Soc. **24**, 273 (2013).

[55] J. C. Maxwell, *A Treatise on Electricity and Magnetism* (Clarendon Press, Oxford, 1873), Vol. 1.

[56] A. Cho, Contact charging of micron-sized particles in intense electric fields, J. Appl. Phys. **35**, 2561 (1964).

[57] M. H. Davis, Two charged spherical conductors in a uniform electric field: Forces and field strength, Q. J. Mech. Appl. Math. **17**, 499 (1964).

[58] E. S. Elton, E. R. Rosenberg, and W. D. Ristenpart, Crater Formation on Electrodes during Charge Transfer with Aqueous Droplets or Solid Particles, Phys. Rev. Lett. **119**, 094502 (2017).

[59] E. S. Elton, Y. V. Tibrewala, and W. D. Ristenpart, Statistical analysis of droplet charge acquired during contact with electrodes in strong electric fields, Langmuir **35**, 3937 (2019).

[60] W. Y. Fowlkes and K. Robinson, in *Particles on Surfaces 1* (Springer, New York, 1988), pp. 143–155.

[61] Trek high-voltage power amplifier model 30/20a, http://www.trekinc.com/products/30-20A.asp (2019), accessed: June 6, 2019.

[62] Microprocessor controller for RH and temperature series 5100/5200, https://www.electrotechsystems.com/wp-content/uploads/2015/10/5100-5200-Manual-Rev0-07-061.pdf (2019), accessed: June 6, 2019.

[63] Alumina particles, http://www.norstoneinc.com/our-products/beads/grinding-media-depot/ (2019), accessed: August 6, 2019.

[64] Edgertronic high-speed video cameras, https://edgertronic.com (2019), accessed: June 6, 2019.

[65] ProAnalyst motion analysis software, https://www.xcitex.com/proanalyst-motion-analysis-software.php (2019), accessed: June 6, 2019.
[66] J. F. Shackelford, Y.-H. Han, S. Kim, and S.-H. Kwon, *CRC Materials Science and Engineering Handbook* (CRC Press, Boca Raton, FL, USA, 2016).
[67] D. J. Lacks and T. Shinbrot, Long-standing and unresolved issues in triboelectric charging, Nat. Rev. Chem. **3**, 465 (2019).
[68] C. Liu and A. J. Bard, Electrostatic electrochemistry at insulators, Nat. Mater. **7**, 505 (2008).
[69] L. S. McCarty and G. M. Whitesides, Electrostatic charging due to separation of ions at interfaces: Contact electrification of ionic electrets, Angew. Chem. Int. Ed. **47**, 2188 (2008).
[70] Y. Zhang, T. Pähtz, Y. Liu, X. Wang, R. Zhang, Y. Shen, R. Ji, and B. Cai, Electric Field and Humidity Trigger Contact Electrification, Phys. Rev. X **5**, 011002 (2015).
[71] V. Lee, N. M. James, S. R. Waitukaitis, and H. M. Jaeger, Collisional charging of individual submillimeter particles: Using ultrasonic levitation to initiate and track charge transfer, Phys. Rev. Mater. **2**, 035602 (2018).
[72] L. Bocquet, E. Charlaix, S. Ciliberto, and J. Crassous, Moisture-induced ageing in granular media and the kinetics of capillary condensation, Nature **396**, 735 (1998).
[73] F. Restagno, L. Bocquet, and T. Biben, Metastability and Nucleation in Capillary Condensation, Phys. Rev. Lett. **84**, 2433 (2000).
[74] J. H. Anderson, Jr., and G. A. Parks, Electrical conductivity of silica gel in the presence of adsorbed water, J. Phys. Chem. **72**, 3662 (1968).
[75] T. Seiyama, N. Yamazoe, and H. Arai, Ceramic humidity sensors, Sens. Actuators **4**, 85 (1983).
[76] Y.-C. Yeh, T.-Y. Tseng, and D.-A. Chang, Electrical properties of porous titania ceramic humidity sensors, J. Am. Ceram. Soc. **72**, 1472 (1989).
[77] C. Cantalini and M. Pelino, Microstructure and humidity-sensitive characteristics of α-Fe_2O_3 ceramic sensor, J. Am. Ceram. Soc. **75**, 546 (1992).
[78] E. Traversa, Ceramic sensors for humidity detection: The state-of-the-art and future developments, Sens. Actuators, B: Chemical **23**, 135 (1995).
[79] K.-S. Chou, T.-K. Lee, and F.-J. Liu, Sensing mechanism of a porous ceramic as humidity sensor, Sens. Actuators, B: Chemical **56**, 106 (1999).
[80] H. Farahani, R. Wagiran, and M. Hamidon, Humidity sensors principle, mechanism, and fabrication technologies: A comprehensive review, Sensors **14**, 7881 (2014).
[81] P. Bai and M. Z. Bazant, Charge transfer kinetics at the solid-solid interface in porous electrodes, Nat. Commun. **5**, 3585 (2014).
[82] R. A. Marcus, Electron transfer reactions in chemistry: Theory and experiment, Rev. Mod. Phys. **65**, 599 (1993).
[83] C. E. Chidsey, Free energy and temperature dependence of electron transfer at the metal-electrolyte interface, Science **251**, 919 (1991).
[84] W. Schmickler and E. Santos, *Interfacial Electrochemistry* (Springer Science & Business Media, New York, NY, USA, 2010).
[85] D. Long and A. Ajdari, Symmetry Properties of the Electrophoretic Motion of Patterned Colloidal Particles, Phys. Rev. Lett. **81**, 1529 (1998).
[86] A. Ajdari, Pumping liquids using asymmetric electrode arrays, Phys. Rev. E **61**, R45 (2000).
[87] E. Yariv, Induced-charge electrophoresis of nonspherical particles, Phys. Fluids **17**, 051702 (2005).
[88] D. Saintillan, E. Darve, and E. S. Shaqfeh, Hydrodynamic interactions in the induced-charge electrophoresis of colloidal rod dispersions, J. Fluid Mech. **563**, 223 (2006).
[89] R. Di Leonardo, Active colloids: Controlled collective motions, Nat. Mater. **15**, 1057 (2016).
[90] J. Yan, M. Han, J. Zhang, C. Xu, E. Luijten, and S. Granick, Reconfiguring active particles by electrostatic imbalance, Nat. Mater. **15**, 1095 (2016).
[91] StarStaX image stacking and blending software, https://markus-enzweiler.de/software/starstax (2019), accessed: June 22, 2019.